


Size-dependent mobility of skyrmions beyond pinning in ferrimagnetic GdCo thin films

Léo Berges , Eloi Haltz , Sujit Panigrahy , Sougata Mallick , Raphaël Weil ,
Stanislas Rohart , Alexandra Mougin , and João Sampaio ^{*}
Université Paris-Saclay, CNRS, Laboratoire de Physique des Solides, 91405 Orsay, France

 (Received 18 July 2022; revised 25 August 2022; accepted 19 September 2022; published 10 October 2022)

Magnetic skyrmions are swirling magnetic textures that can be efficiently driven with spin-orbit torques with a deflected trajectory. However, pinning slows skyrmions down and alters their trajectory, which prevents a quantitative comparison to analytical models. Here, we study skyrmions driven by spin-orbit torques at room temperature in ferrimagnetic GdCo thin films, an amorphous material with low pinning. Above a sharp current depinning threshold, we observe a clearly linear velocity increase with current that extrapolates to zero and a constant deflection angle, reaching high velocities up to 200 m/s. The mobility increases and the depinning threshold current decreases with the skyrmion diameter, which we vary using an external magnetic field. An analytical model based on the Thiele equation quantitatively reproduces these findings with a single fitting parameter. This validates the linear flow regime description and shows, in particular, the important role of skyrmion size in its dynamics.

DOI: [10.1103/PhysRevB.106.144408](https://doi.org/10.1103/PhysRevB.106.144408)

I. INTRODUCTION

Magnetic skyrmions are particlelike magnetic textures similar to magnetic bubbles [1,2], from which they differ by their well-defined chirality and nontrivial topology. In the past decade, advances in the optimization of the interfacial Dzyaloshinskii-Moriya interaction (DMI) and of current-induced spin-orbit torques (SOTs) have allowed the stabilization of extremely small skyrmions, down to tens of nm, and their efficient driving in thin-film tracks [3–5]. Their chirality is a crucial element to SOT driving, while their nontrivial topology manifests itself by a deflected trajectory.

Three regimes for skyrmion motion can be distinguished with increasing driving current: a pinning regime, where the effects of the film inhomogeneities are strong; a linear flow regime, where the skyrmion propagates while conserving its shape; and a nonlinear flow regime, where the skyrmion shape is deformed. In the flow regime, analytical and numerical models [6,7] describe the skyrmion dynamical laws and identify the main governing parameters: the current density (J), the skyrmion size, and the material's angular momentum density (L_S). The skyrmion velocity is expected to increase linearly with current density, while the deflection should stay constant [8,9]. As a function of skyrmion size, the velocity is expected to increase whereas the deflection should decrease. The deflection should be proportional to L_S , which has motivated an interest in antiferromagnetic or ferrimagnetic materials where L_S can be zero and the skyrmion deflection suppressed.

However, in most studied systems, the effects of pinning are significant even at the highest applied current densities. Pinning slows down skyrmions, stops their motion below

a certain threshold, and interferes with their deflection and shape [6,10]. The flow regime, where the skyrmion should propagate with negligible effects from pinning and thus with high mobility, is often inaccessible due to the limitations that Joule heating imposes on the applied current density. Experimental observations, therefore, agree only partially with these predictions or are incomplete. For example, instead of being constant, the deflection has most often been observed to increase with current, eventually saturating at the highest currents [4,5,11,12]. The velocity was observed to increase linearly with current in some experiments [13,14], but often follows a shifted linear law [3,5,15,16] or even a highly nonlinear variation with current, quantitatively slower than the velocity expected for the linear regime [4,12,17,18]. The dependence of the deflection angle on the diameter was observed in some cases [4,14] but not in others [18]. The dependence of the velocity with diameter was found to be constant in Ref. [19]. The variation of the deflection angle with L_S was observed for domains with chiral domain walls [20], but not for isolated skyrmions.

Here, we study the SOT-driven dynamics of skyrmions in a thin film of GdCo, a rare-earth/transition-metal (RETM) ferrimagnetic alloy. The high sensitivity of magnetization (M_S) to temperature and alloy composition in RETMs [21] is used to tune the stability of skyrmions near room temperature. The very low pinning of this amorphous material allows us to study the skyrmion dynamics in the flow regime and to attain higher mobility than what was observed in other thin films. The variation of the skyrmion mobility and deflection with current density and skyrmion diameter is studied. These observations are compared quantitatively to an analytical model based on the Thiele equation. We also study the pinning threshold and its evolution with the skyrmion size, which is compared to previous predictions based on simulations of inhomogeneous systems.

^{*}joao.sampaio@universite-paris-saclay.fr

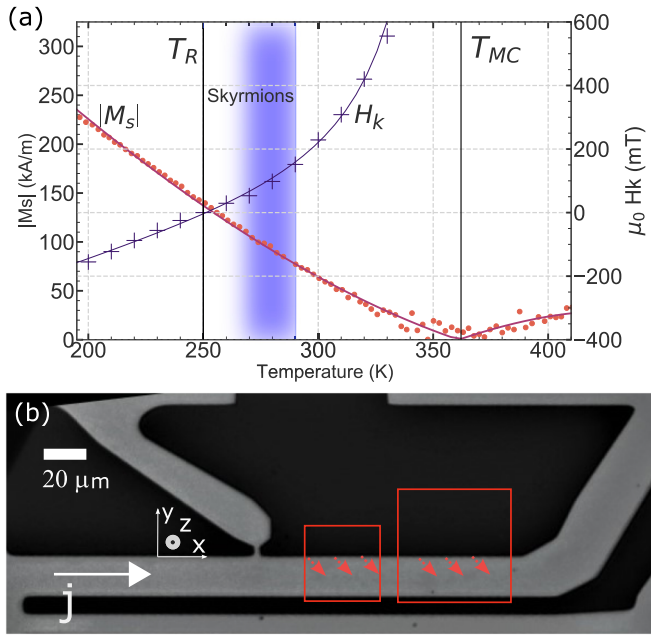


FIG. 1. (a) Saturation magnetization $|M_S|$ (red dots measured by SQUID; the line is given by the mean-field model) and effective anisotropy field H_k (measured from AHE loops). The temperature range highlighted in blue shows where skyrmions were observed at low or zero magnetic field. (b) Optical image of the device. The magnetic track appears in light gray. The two red squares delimit the field of view of the skyrmion tracking measurements. The red arrows indicate the typically observed nucleation side and the propagation direction of skyrmions.

II. RESULTS

A Ta(1)/Pt(5)/Gd_{0.32}Co_{0.68}(5)/Ta(3) (thicknesses in nm) thin film was deposited by e-beam evaporation in an ultrahigh-vacuum chamber [22] on a Si/SiO_x (100 nm) substrate, and patterned as 20- μ m-wide tracks [Fig. 1(b)]. The magnetization of the film (M_S) versus temperature (T) was measured by SQUID [Fig. 1(a)], showing a strong variation typical of RETM ferrimagnets [21]. It shows a magnetic compensation temperature $T_{MC} = 360$ K, at which the magnetic moments of the two antiferromagnetically coupled sublattices (Gd and Co) balance out and $M_S = 0$. Analogously, the angular momenta of the sublattices balance out at the angular momentum compensation temperature, T_{AC} , which we expect to be about 425 K. The effective anisotropy field (H_k), shown in Fig. 1(a), was extracted from fits of anomalous Hall effect (AHE) hysteresis cycles taken with a tilted field [23]. The fitted H_k increases with temperature up to 360 K, and is negative below 250 K. The point of $H_k = 0$ defines the reorientation temperature T_R , where the anisotropy changes from a hard ($T < T_R$) to an easy ($T > T_R$) perpendicular axis.

The hysteresis cycles with a perpendicular field taken at different temperatures below T_{MC} were measured using the magneto-optical Kerr effect (MOKE) and are shown in Fig. 2(a). Because the measured MOKE signal is mostly due to the Co sublattice [21,22] and $T < T_{MC}$, a positive saturation is observed at negative applied magnetic field, and it corresponds to a Co magnetization pointing along $+\hat{z}$ [in the

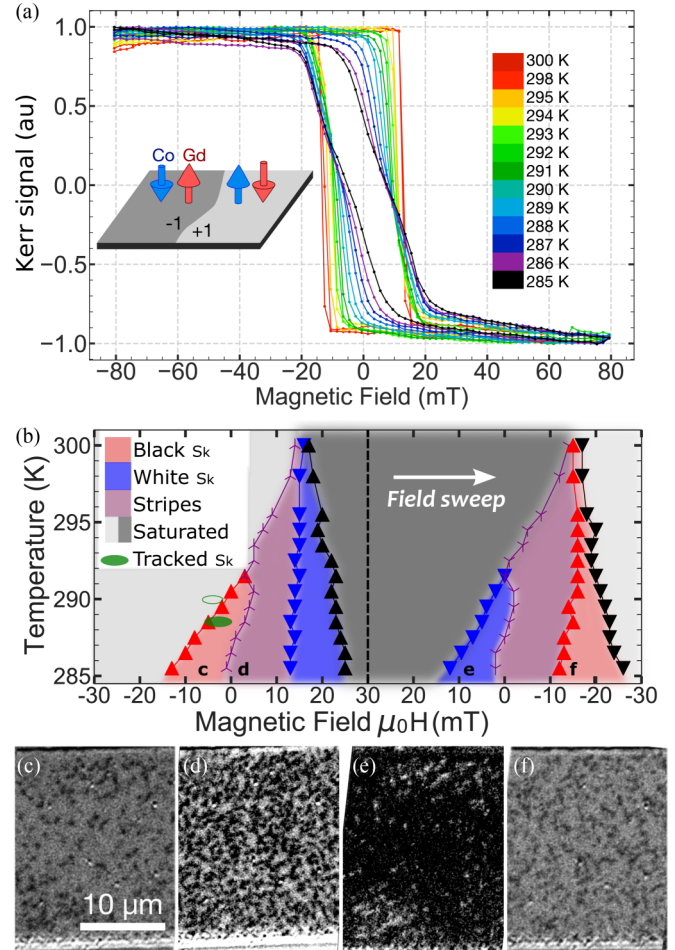


FIG. 2. (a) MOKE hysteresis loops near the temperature range of skyrmion stability. Inset: Diagram of the orientation of the Co and Gd sublattices in the domains and corresponding Kerr signal. (b) Phase diagram of magnetic textures during field hysteresis loops from -30 to 30 mT and back to -30 mT. The phases and their transition fields are defined in the text. Red, blue, and black triangles and purple stars correspond to the phase-transition fields in the 13 measured field sweeps from which the phase borders (lines) are deduced. The green empty and filled regions correspond to the two temperatures of the skyrmion dynamics measurements. (c)–(f) MOKE differential images at $T = 285.5$ K and at the magnetic fields indicated in (b).

coordinate system of Fig. 1(b)] and a net magnetization along $-\hat{z}$. By convention, we describe the orientation of the magnetic film using the orientation of the Co [24]. Slightly above T_R and below 290 K, the hysteresis cycles present a peculiar shape with low remanence which is a sign of a multidomain state containing textures such as stripes or skyrmions.

The MOKE images taken during the hysteresis loops reveal different types of textures, which we classify in four phases, shown in Fig. 2(b): saturated, black or white skyrmions (with the cobalt moment at the center along $-\hat{z}$ or $+\hat{z}$, respectively), and stripes. The transition from skyrmions to stripes [shown as lines and symbols in Fig. 2(b)] is smooth. To distinguish them, we extract the shapes of the domains from the images using a watershed segmentation algorithm [25], and we calculate their surface-to-perimeter ratios. A threshold was chosen to

classify the textures either as stripes (with higher ratio) or skyrmions (with lower ratio). Similar results were obtained by using the eccentricity of the best-fitting ellipse (with a different threshold).

Starting with a saturated state at -30 mT and increasing the field, we observe skyrmions [black dots in the MOKE image of Fig. 2(c)] above a temperature-dependent nucleation field (first red triangles). Then a phase of labyrinthlike stripes occurs, which become denser with increasing positive field [Fig. 2(d)]. The white stripes are then compressed into sparse white skyrmions (Co moment along $+\hat{z}$) before reaching the full saturation of the sample. A symmetric evolution is observed along the opposite field sweep [Figs. 2(e) and 2(f)].

Skyrmions are only observed above T_R and on a narrow range of field, which is narrower for higher temperatures. When dipolar energy is important and the skyrmion diameter is large, its stability can be understood by using the analysis developed for magnetic bubbles [1] and later refined for the skyrmion case [26–28]. As a first approximation, skyrmions or stripes are expected when the characteristic dipolar length $l_c = \sigma / (\mu_0 M_s^2)$ (where σ is the domain wall energy) is greater than or comparable to the film thickness. This is indeed the case near 290 K (see Appendix D), where spontaneous textures are observed.

The skyrmions show different sizes and shapes. To analyze them, we define the skyrmion diameter, \varnothing , as the one of a circle with the same surface. The measured \varnothing are often close to the optical resolution. To validate our procedure, MOKE images were compared with high-resolution measurements of magnetic force microscopy (MFM) of the same skyrmions, shown in Figs. 3(b) and 3(c). Depending on the algorithm threshold parameter, we obtain $\varnothing = 0.4 \pm 0.1 \mu\text{m}$ for the small skyrmion in the image (compared to 380 nm in MFM) and $\varnothing = 1.0 \pm 0.1 \mu\text{m}$ for the larger skyrmion (900 nm in MFM), which validates the use of MOKE at least down to $0.4 \mu\text{m}$.

Figure 3(a) shows the histograms of skyrmion diameters at two different applied fields (at $T = 288.5$ K). At $B = -1$ mT, an average diameter of $\langle \varnothing \rangle = 852$ nm and a standard deviation of 230 nm are obtained. The rather large size distribution is explained by the effects of pinning [29] coupled to the very low domain-wall energy near T_R , which led to a very shallow energy versus size profile [28]. The size also shows a hysteretic behavior with field, shown in Fig. 3(d) for black skyrmions during a minor hysteresis loop. This is also compatible with the effects of pinning [29–31]: during the positive field sweep, the skyrmion enlarges but does not attain the equilibrium diameter due to pinning. The opposite happens when the field decreases, which results in the shown hysteretic behavior, where the equilibrium diameter is inside the hysteretic gap. A clear decrease of the average size with field is obtained. A numerical micromagnetic study reproduces this trend (see Fig. 6 in Appendix C).

III. DYNAMICS UNDER CURRENT

We studied the skyrmion current-driven dynamics in a $20\text{-}\mu\text{m}$ -wide magnetic track [Fig. 1(b)] and focused on sparse skyrmions after saturating the sample with a negative field ($T = 285.5$ K; see the supplemental material [23] for 290 K).

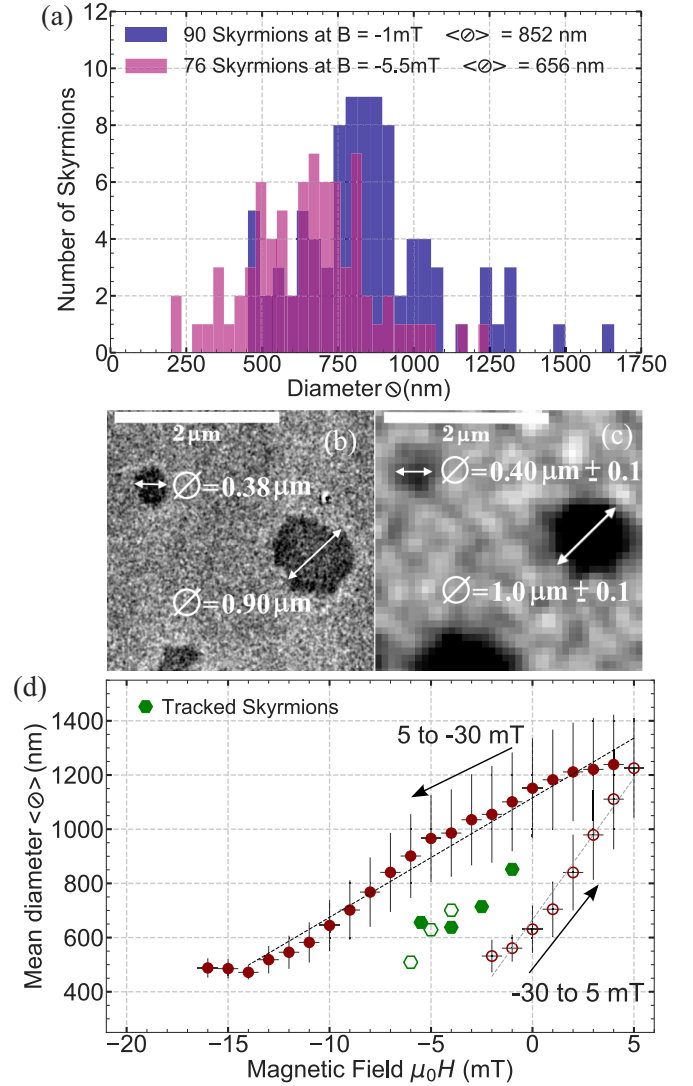


FIG. 3. (a) Skyrmion diameter histogram for two magnetic fields at $T = 288.5$ K. (b) MFM and (c) MOKE images of the same area showing two skyrmions. (d) Full and empty red circles show the average skyrmion size vs magnetic field applied along $+\hat{z}$ for $T = 288.5$ K. Green filled (empty) hexagons show the sizes for the tracked skyrmions at 288.5 K (290 K). The error bars are the standard deviation of sizes measured in the images. Due to the Faraday effect during the field sweep, the binarization threshold is field-dependent.

10-ns electrical pulses of various current densities J were applied, and the size and position of the skyrmions were tracked with MOKE images. After the pulse, skyrmions were nucleated most often on the edges, which act as defects, and most often on the side favored by the Oersted field [23]. Note that skyrmions can be nucleated by current even in states that were initially saturated after the field sweep [green ellipses in Fig. 2(b)]. The velocity is calculated from the skyrmion center position before and after the pulse. A single pulse was injected between images for the fastest skyrmions, whereas 5–1000 pulses were injected for the slowest skyrmions (at a low repetition rate, 50 Hz, ensuring no cumulative Joule heating effect).

We have tracked a large number of skyrmions using a semiautomated process consisting in manually identifying the same skyrmion in successive images and automatically measuring their size, velocity, and deflection angle. Some 800 skyrmions were tracked along 2500 images, giving an average of three images per determined velocity at two different temperatures for several magnetic fields. This large number of skyrmions drastically improves the precision of the data analysis even with a significant dispersion of skyrmion size and velocity.

The inset in Fig. 4(a) shows the parallel trajectories of three black skyrmions (with Co moment along $-\hat{z}$) over five successive superimposed images. Note that some skyrmions disappear and are not present in the last images. Indeed, most skyrmions disappear after a few frames, and only a few cross the entire track, especially beyond the region where the Oersted field is opposite to the skyrmion core [23]. Skyrmions move along the current direction (\hat{x}), opposite to the flow of electrons, which is coherent with the SOT and chirality given by a Pt buffer layer. The presence of SOT is confirmed by torque measurements [23]. There is a significant deflection towards $-\hat{y}$, which we attribute to the gyrotropic force related to the skyrmion topology [32]. Note that it is opposite to that of a skyrmion with same cobalt core orientation in a pure cobalt film [4,15]. Indeed, the gyrotropic deflection is expected to be proportional to the L_S of material, which is negative in this GdCo film below T_{MC} , opposite to that of a pure Co film.

Figures 4(a) and 4(b) show the skyrmion velocity and deflection angle versus current density, J , at three values of applied magnetic field. We observe, at low J , a hopping regime of very few moving skyrmions with a badly defined deflection angle and very slow velocity. This is followed by an abrupt transition at a depinning current density J_D above which most skyrmions propagate and obey a linear velocity regime that extrapolates to zero. These skyrmions move up to 170 m/s (on average) for the largest current density of $J = 290 \text{ GA/m}^2$ and $B = -1 \text{ mT}$, resulting in a mobility of $0.59 \text{ ms}^{-1}/\text{GA m}^{-2}$.

Skyrmions display a large deflection angle of $-40^\circ \pm 10^\circ$ once the linear regime is reached. During the depinning regime, the angle is found to be larger. However, only a few skyrmions moved in these conditions and were mostly located near the edge of the track, which may strongly bias the measurement of the angle. The angle seems also to increase at the largest current densities, which may be due to an effect of shape distortions [16].

The mobility and J_D are observed to vary with the applied magnetic field: The lowest $J_D = 125 \text{ GA/m}^2$ and highest mobility are observed for the lowest field (-1 mT). No clear effect of the field on the deflection angle can be discerned.

The average size of the tracked skyrmions [green hexagons in Fig. 3(d)] decreases with increasing magnetic field, as expected. Also, the size of the tracked skyrmions is within the hysteretic gap of the sizes measured during field sweep, which indicates that they are close to the equilibrium diameter for that applied field (as the equilibrium diameter is inside the hysteretic gap). Note, however, that the images capture the skyrmion tens of ms after the pulse, and so the measured size may differ from the size during motion. We observe the

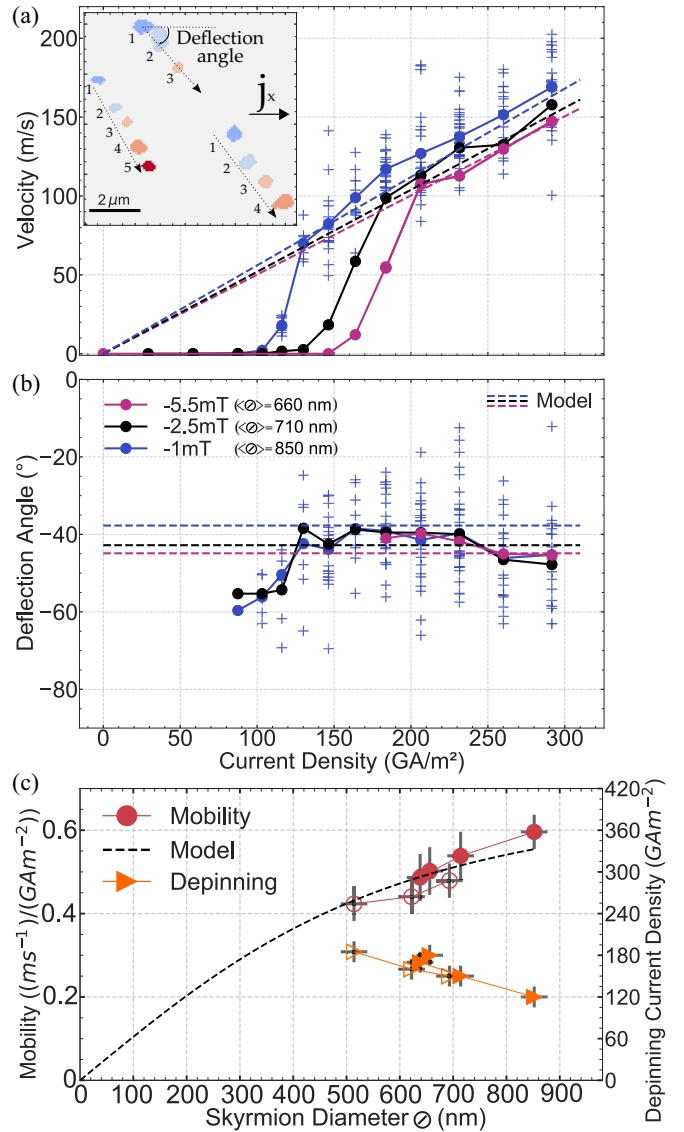


FIG. 4. (a),(b) Skyrmion velocity and deflection angle vs current density, obtained for three different magnetic fields. The line and circles are the mean values of all tracked skyrmions, and the crosses are the measurements for individual skyrmions (only shown for -1 mT for clarity). The inset in (a) shows the superposition of the binarized images after five successive 10-ns-long pulses of 210 GA/m^2 showing three propagating skyrmions. (c) Skyrmion depinning current density and mobility vs skyrmion diameter measured at 288.5 K (filled markers) and 290 K (empty markers). The dashed lines in (a)–(c) correspond to the values calculated by the model.

lowest depinning current J_D and the highest velocity for the smallest applied magnetic field, i.e., for the largest skyrmions. The relation between the dynamic features and the magnetic field might thus be attributed to the change in skyrmion size [Fig. 4(c)]. As for depinning, previous simulation studies of skyrmions pinned in granular films [10,33] predict that the pinning threshold varies strongly with skyrmion size and attains a maximum when the diameter is comparable to the lengthscale of the variation of magnetic parameters. The presented data show a strong variation of pinning with size in an amorphous film, suggesting that the conclusions of those

studies may also be applied to inhomogeneous films other than multicrystalline materials. The observed variation of J_D with diameter is compatible with a characteristic pinning length smaller than the observed diameters. Although not directly comparable, microscopy cross-section observations of a similar material (GdFeCo) deposited in the same conditions [34] showed lateral inhomogeneities with a lengthscale around 3 nm, suggesting that the pinning lengthscale of this film is indeed smaller than the observed diameters.

The observed velocity and mobility are significantly higher than what has been observed in other thin films (see Ref. [13] for GdFeCo and, for other materials, e.g., [3–5,14]). As we are far from T_{AC} , this high mobility is not due to the particularities of ferrimagnetic dynamics, but is mainly due to the fact that the skyrmions attain the linear velocity regime due to the weak pinning of this material, whereas most other skyrmion propagation observations were performed below or near the pinning threshold. Another factor for the lower mobility reported in previous studies is the smaller skyrmions that were studied, as is discussed in the following section.

IV. MODELING SKYRMION DYNAMICS

To examine the effect of the size on the skyrmion velocity and deflection, we use a model based on the Thiele equation, which describes the motion of rigid magnetic textures [32,35]. This model, described in detail in Appendix A, yields the skyrmion velocity

$$|v| = \frac{|v_0|}{\sqrt{1 + \rho^2}}, \quad (1)$$

where ρ is the deflection rate [the deflection angle is $\arctan(\rho)$] and v_0 is the velocity without deflection, given by

$$v_0 = -\frac{\hbar J \theta_{\text{SHE}} f}{2eL_\alpha t d} \quad \text{and} \quad \rho \equiv \frac{v_y}{v_x} = \frac{L_S n}{L_\alpha d}, \quad (2)$$

where $L_S = M_S/\gamma$ is the net angular moment density (negative as $T < T_{AC}$, as discussed earlier), L_α is the energy dissipation rate [36,37], θ_{SHE} is the spin Hall angle, t is the film thickness, e is the elementary charge, and \hbar is the reduced Planck's constant. The parameters n , f , and d are given by spatial integrals of the skyrmion magnetization profile (see Appendix A). In particular, f and d depend on its radius.

In the limit of small radius compared to domain-wall width, the model predicts that $v_0 \propto f/d \propto R$ and that $\rho \propto n/d \rightarrow 1$ (its maximum). In the large radius limit, v_0 is independent of R and $\rho \propto 1/R$. Therefore, the velocity v [Eq. (1)] is expected to increase and saturate with skyrmion size, while the deflection angle should be constant for small skyrmions and then decrease. For a given radius, this model, which does not account for pinning, predicts a linear dependence of the velocity with current and a constant deflection angle.

To apply the model to our observations, we characterized the material parameters using Brillouin light scattering (BLS) measurements [23]. The mobility $\mu = |v|/J$ [Fig. 4(c)] was fitted with this model with only θ_{SHE} as a free parameter (which is only a scaling factor), found to be in the range of the experimental value obtained from torque measurements [23,38]. The model predictions with these parameters are shown by the dashed lines in Fig. 4. They reproduce the

size dependence of the linear velocity regime of skyrmions taken at 288.5 and 290 K. The predicted deflection angles are consistent with the data, but the agreement is less satisfactory, in the sense that the expected variation of deflection angle with diameter is not observed in experimental angles. Moreover, for the skyrmion sizes we observe ($R/\Delta = 15$), we expect the mobility variation with size to be driven only by the variation of ρ . Therefore, the variation of mobility implies a variation of deflection that is not observed. This may be due to the dispersion of the measured deflection angle, which can blur the variation with size. The model also predicts the angle to be more dispersed than the velocity v for a given size distribution [23]. Another cause may be due to the effects of skyrmion-skyrmion interactions, which the model does not account for [19,39,40].

V. DISCUSSION AND CONCLUSION

We observe skyrmions in a RETM ferrimagnetic thin film, at room temperature and close to T_R with zero external magnetic field. Skyrmions are driven by SOT and follow a clear linear regime after a steep depinning threshold, which decreases with the skyrmion size. The flow regime, beyond the effects of pinning, was observed, with a linear dependence of the velocity extrapolating to zero. The mobility, its dependence on the skyrmion size, and the trajectory deflection angle were found to be in quantitative agreement with an analytical model based on the Thiele equation, with a single fitting parameter. This shows that the rigid skyrmion model using the Thiele equation is sufficient and quantitative, as long as the skyrmion is unhindered by pinning and even for the largest current density that was applied. In particular, the model predicts a strong reduction of mobility at smaller diameters, which is potentially a problem for the scaling down skyrmion devices.

The observed large mobility and low pinning show the promise of RETM ferrimagnets as tunable systems to explore and optimize the complex skyrmion static and dynamical properties. Indeed, in RETMs, changing temperature or composition changes substantially the net magnetization and angular momentum, which can be used to control the skyrmion size and stability as well as its dynamics. We observed a negative deflection angle in a film below T_{AC} , i.e., with negative net L_S , opposite to the deflection of a pure Co film. This supports the prediction that the gyrotropic deflection is determined by L_S , and that deflectionless skyrmions should be achievable at T_{AC} .

ACKNOWLEDGMENTS

The authors thank André Thiaville for the fruitful discussions and the study of the sample properties by BLS. This work was supported by a public grant overseen by the French National Research Agency (ANR) as part of the “*Investissements d’Avenir*” program (Labex NanoSaclay, reference: ANR-10-LABX-0035, project SPICY) and by an Indo-French collaborative project supported by CEFIPRA (IFC/5808-1/2017). Magnetometry and Anomalous Hall effect measurements were performed at the LPS Physical Measurements Platform.

APPENDIX A: THIELE EQUATION FOR SKYRMION DYNAMICS

Under the hypothesis of a rigid (or stationary) profile $\mathbf{m}(\mathbf{r}, t) = \mathbf{m}_0(\mathbf{r} - \mathbf{v}t)$, where $\mathbf{m}_0(\mathbf{r})$ is the rigid texture and \mathbf{v} its velocity, the skyrmion dynamics can be described with the Thiele collective coordinate model [32,35], obtained by spatially integrating the Landau-Lifshitz-Gilbert (LLG) equation. For a circular Néel skyrmion subjected to a force induced by a current \mathbf{J} along the x direction, the Thiele equation reads [32,35]

$$\mathbf{G} \times \mathbf{v} - \alpha D \mathbf{v} + \mathbf{F} = 0, \quad (\text{A1})$$

where $\mathbf{G} = L_S t n \hat{\mathbf{z}}$, $\alpha D = L_\alpha t d$ ($\alpha = L_\alpha/L_S$ is Gilbert's damping constant), and $\mathbf{F} = -\frac{\hbar}{2e} \theta_H \mathbf{J} f$. The three terms in Eq. (A1), respectively, arise from the precessional, damping, and SOT terms in the LLG equation. The parameters n , d , and f characterize the texture geometry $\mathbf{m}_0(\mathbf{r})$ and are given by

$$n = \iint \left(\frac{\partial \mathbf{m}_0}{\partial x} \times \frac{\partial \mathbf{m}_0}{\partial y} \right) \cdot \mathbf{m}_0 d^2 r, \quad (\text{A2a})$$

$$d = \iint \left(\frac{\partial \mathbf{m}_0}{\partial x} \right)^2 d^2 r, \quad (\text{A2b})$$

$$f = \iint \left(m_{0,x} \frac{\partial m_{0,z}}{\partial x} - m_{0,z} \frac{\partial m_{0,x}}{\partial x} \right) d^2 r. \quad (\text{A2c})$$

They correspond, respectively, to the texture topology, to the magnetization rotation length-scale, and to the texture chirality.

The solution of Eq. (A1) is

$$v = \|\mathbf{v}\| = |v_0|/\sqrt{1 + \rho^2}, \quad (\text{A3a})$$

$$v_y/v_x = \rho, \quad (\text{A3b})$$

with

$$v_0 = \frac{F}{\alpha D} = -\frac{\hbar j \theta_H}{2e \alpha L_S t d} f, \quad (\text{A4a})$$

$$\rho = \frac{G}{\alpha D} = \frac{1}{\alpha} \frac{n}{d}, \quad (\text{A4b})$$

where v_0 and ρ correspond, respectively, to the velocity along the current direction (i.e., the velocity when $v_y = 0$) and to the deflection of the skyrmion.

In a ferrimagnet where the coupling between sublattices is strong, a perfect antiparallel alignment of the two sublattices can be assumed: $\mathbf{m} = \mathbf{m}^{\text{Co}} = -\mathbf{m}^{\text{Gd}}$, where we set by convention the effective normalized magnetization parallel to the Co moment. In this case, we can apply this result by using the effective model introduced by Wangsness and others [24,36].

A two Thiele equation model, developed in [23], shows that this effective approach is valid even in the case of imperfect antiparallel alignment. In the effective model, the material parameters are related to the parameters of each sublattice: the net magnetization is $M_S = M_S^{\text{Co}} - M_S^{\text{Gd}}$, the net angular momentum is $L_S = L_S^{\text{Co}} - L_S^{\text{Gd}}$, the energy dissipation rate is $L_\alpha = \alpha^{\text{Gd}} L_S^{\text{Gd}} + \alpha^{\text{Co}} L_S^{\text{Co}}$, and the effective Hall angle is $\theta_H = \theta_H^{\text{Gd}} + \theta_H^{\text{Co}}$ [36] (the parameters labeled ‘‘Co’’ or ‘‘Gd’’ refer to the parameters of each sublattice). M_S and L_S , and their variation with temperature, can be calculated with a mean-field model [Fig. 1(a)]. As is common in RETMs, θ_H^{Gd} can be

neglected. The effective α diverges at T_{AC} ($\alpha = L_\alpha/L_S$), and so it is convenient to use the always-finite L_α instead. The f , d , and n parameters are unchanged as they are purely functions of the texture's morphology. We can then rewrite Eqs. (A4) as

$$v_0 = -\frac{\hbar j \theta_H}{2e L_\alpha t d} f, \quad (\text{A5a})$$

$$\rho = \frac{L_S}{L_\alpha} \frac{n}{d}. \quad (\text{A5b})$$

This formalism successfully describes the vanishing gyrotropic deflection expected at the angular momentum compensation T_{AC} (where $L_S = 0$) [13,20,41]. The velocity modulus displays a maximum at T_{AC} with $|\mathbf{v}| \approx |v_0|(1 - \frac{1}{2}\rho^2)$.

APPENDIX B: EFFECT OF SKYRMION SIZE ON THIELE PARAMETERS

A strong variation of the dynamics with the geometric parameters in Eqs. (A2) is expected when the skyrmion radius is comparable to the domain-wall width parameter $\Delta = \sqrt{A/K_{\text{eff}}}$ (with A the exchange stiffness and K_{eff} the effective anisotropy). This is important near T_R , as in the experiments, where Δ can be large. Since n corresponds to the skyrmion topological number, it is independent of the skyrmion size ($n = \pm 4\pi$ depending on the skyrmion core polarity). The integral d is similar to the micromagnetic exchange integral [32,42], and it is expected to scale likewise with the skyrmion size. The integral that defines f is similar to a micromagnetic Dzyaloshinskii-Moriya integral [43] and therefore involves the skyrmion chirality c ($c = \pm 1$, respectively, for clockwise and counterclockwise spin rotation). In the limit of $R \gg \Delta$, $f \rightarrow \pi^2 c R$. Since $f \rightarrow 0$ for small skyrmions, this linear variation can be used as an approximation for the full range of size. We also note that it is independent of Δ . The variation of these three parameters with the skyrmion radius is shown by the lines in Figs. 5(a) and 5(b).

For a skyrmion radius R large as compared to Δ , $d = 2\pi R/\Delta$ [15,44]. However, as shown by Belavin and Polyakov [45], an exchange integral does not vanish at small size for a topological texture [45], and, for $R \rightarrow 0$, $d \rightarrow |n|$, which shows that the dissipation does not vanish at small sizes [46]. To describe the dissipation over the full range of R , the two limits can be interpolated as

$$d \approx |n| \exp\left(-\frac{2\pi R}{|n|\Delta}\right) + \frac{2\pi R}{\Delta}. \quad (\text{B1})$$

This approximation is shown as dashed lines in Fig. 5. As a consequence, the mobility, which is proportional to f/d [Eq. (A5)], vanishes for small skyrmions [Fig. 5(d)], and the deflection is maximum but does not diverge [Fig. 5(c)].

APPENDIX C: MICROMAGNETIC SIMULATIONS

We performed micromagnetic simulations of skyrmions in a GdCo thin film using MuMax³ [47], modified to account for the specificity of ferrimagnetic films [23,36,48], each lattice being described independently, and coupled with an antiferromagnetic coupling $J_{\text{TM/RE}}$. The parameters used for the

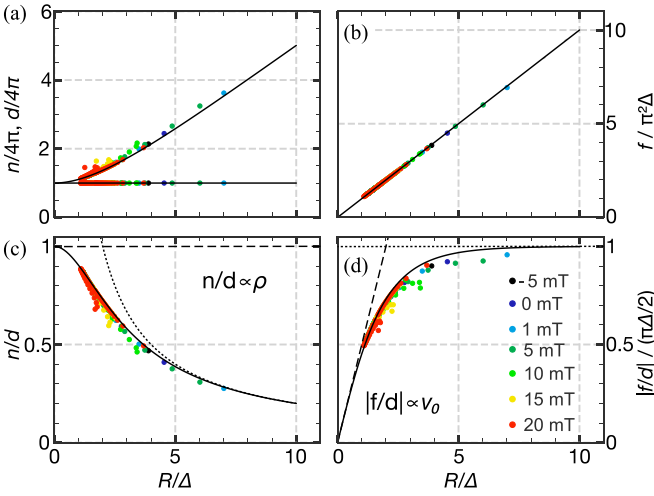


FIG. 5. Geometric components of the Thiele parameters vs the normalized skyrmion radius (R/Δ). (a) Gyrotropic n and dissipation d parameters. (b) Spin Hall effect force related length f (divided by Δ) so that it is represented as a function of R/Δ . (c) n/d , proportional to the skyrmion deflection ρ . (d) f/d , proportional to the skyrmion deflectionless velocity v_0 . The solid lines correspond to the analytical expressions in the text, and the dots correspond to the simulations of a GdCo ferrimagnetic alloy at different fields and temperatures. Note that Δ is not constant (Fig. 6). In (c) and (d), the dashed line shows the small skyrmion limit ($n/d = 1$, $|f/d| = \pi R/2$) and the dotted line shows the large skyrmion limit ($n/d = 2\Delta/R$, $|f/d| = \pi \Delta/2$).

simulations (Table I) are those corresponding to the skyrmions phase in Fig. 1. We keep all parameters constant in temperature except for the sublattice magnetization and angular momentum [$M_S^{\text{Co}}(T)$, $M_S^{\text{Gd}}(T)$ calculated with the mean-field model, Fig. 1(a); $L_S^{\text{Co}} = M_S^{\text{Co}}(T)/\gamma_{\text{Co}}$, $L_S^{\text{Gd}} = M_S^{\text{Gd}}(T)/\gamma_{\text{Gd}}$].

The simulated skyrmion radius versus temperature shows a minimum at T_{MC} (Fig. 6). As observed experimentally, the external field changes the size of the skyrmion. This effect is opposite above and below T_{MC} as the net magnetization of the skyrmion core changes sign. The temperature of the minimum radius is, therefore, shifted by the field.

The skyrmion velocity versus temperature and field is shown in Fig. 7(a). These simulations are performed in a

TABLE I. Parameters used for the micromagnetic simulations. Only the M_S and L_S of the two sublattices were considered to vary with temperature according to the mean-field model [Fig. 1(a)]. Their range is shown in brackets. $J_{\text{TM/RE}}$ is the interlattice coupling, and g is the g -factor ($\gamma = g\mu_B/\hbar$, where μ_B is the Bohr magneton).

	Co	Gd
g	2.22	2.00
α	0.019	0.019
M_S (MA/m)	[0.62–0.5]	[1.1–0.4]
K (kJ/m ³)	11.5	0
A (pJ/m)	4.6	0
D_{DMI} (mJ/m ²)	0.22	0
$J_{\text{TM/RE}}$ (MJ/m ³)		25
θ_{SHE}	0.03	0

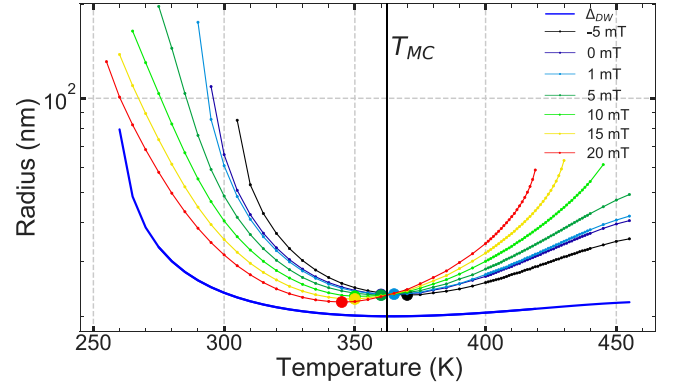


FIG. 6. Skyrmion radius vs temperature at several magnetic fields. The circles represent the minimum radius of each field.

low current regime ($J = 100 \text{ GA/m}^2$) so that the skyrmion is not deformed. A velocity maximum is observed close to T_{AC} , as predicted by the model. However, the velocity curve is more complex than a simple peak. Since the mobility depends on the radius, and therefore on the temperature, the result is affected by both the skyrmion size and the angular momentum compensation. The mobility minimum at T_{MC} is due to the size minimum (Fig. 6). The maximum observed slightly above T_{AC} is due to a combination of vanishing L_S and the increasing size with temperature. The model, using no fitting parameters other than the static skyrmion diameter (obtained from simulations), is in quantitative agreement with

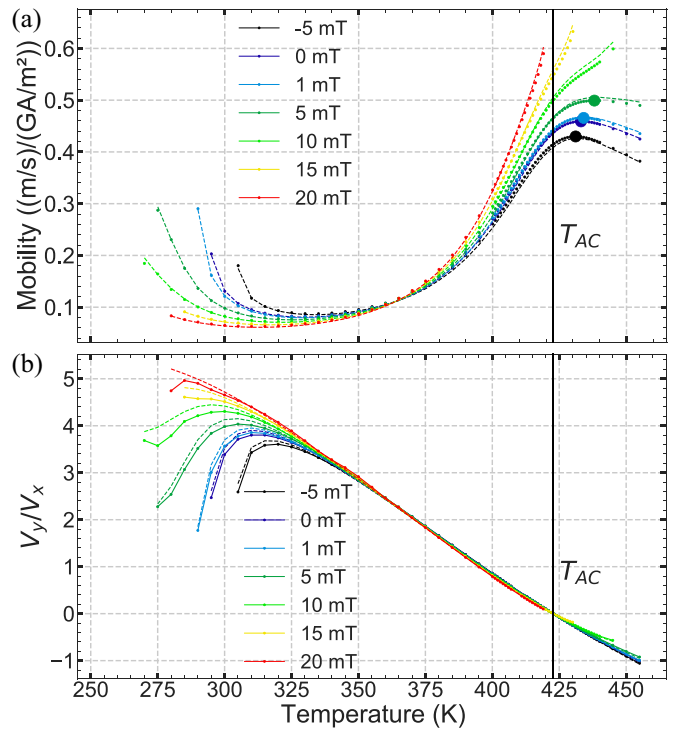


FIG. 7. (a) Mobility $|v|/J$ vs temperature for different magnetic fields from simulations (points) and model (dashed lines). The circles represent the maximum mobility for each field. (b) Deflection v_y/v_x vs temperature and field. $J = 100 \text{ GA/m}^2$.

TABLE II. Sample magnetic parameters. M_S measured by SQUID [Fig. 1(a)], H_k extracted from AHE measurements [23]. The dipolar characteristic length is $l_c = \frac{\sigma}{\mu_0 M_S^2}$, where $\sigma = 4\sqrt{AK_{\text{eff}}}$ – πD_{DMI} is the domain wall energy.

	280 K	290 K	300 K
M_S (kA/m)	90	78	65
K_{eff} (kJ/m ³)	6.4	7.7	8.8
l_c (nm)	–0.4	8	22
D_c (mJ/m ²)	0.22	0.24	0.26
Δ (nm)	27	24	23

the simulations, a consequence of the simulated skyrmion conserving its static profile during motion and despite the finite coupling (the case of imperfect antiparallel alignment is treated in [23]). The skyrmion deflection v_y/v_x crosses zero at T_{AC} and is linear around T_{AC} . This supports the model, which predicts that $v_y/v_x \propto L_S$. Far from T_{AC} , the deflection deviates

from this linear relation due to the large skyrmion size, as the deflection decreases as $1/R$.

APPENDIX D: MATERIAL PARAMETERS

We determined some of the material parameters using Brillouin light scattering measurements [23,49]: exchange stiffness $A = 4.6$ pJ/m, the DMI parameter $D_{\text{DMI}} = -0.22$ mJ/m² (which yields a surface DMI parameter $D_S = 1.1$ pJ/m), $\gamma/2\pi = 18.3$ GHz/T, and $\alpha = 0.15$. The exchange stiffness A was found to be in agreement with [50,51]. We can evaluate how these measurements compare to the expected effective values given by the Wangsness theory. The value of γ is much lower than the value of Co, as expected from the Wangsness formula. We expect that the measured effective α to be larger than the α of the Co sublattice, which is indeed the case [52].

Table II shows the calculated l_c and critical DMI parameter $D_C = 4\sqrt{AK_{\text{eff}}}/\pi$ at which stripes are favored, calculated for three temperatures.

- [1] C. Kooy and U. Enz, Experimental and theoretical study of the domain configuration in thin layers of BaFe₁₂O₁₉, *Philips Res. Rep.* **15**, 7 (1960).
- [2] A. Malozemoff and J. Slonczewski, *Magnetic Domain Walls in Bubble Materials*, *Applied Solid State Science* (Academic Press, New York, 1979).
- [3] S. Woo, K. Litzius, B. Krüger, M. Y. Im, L. Caretta, K. Richter, M. Mann, A. Krone, R. M. Reeve, M. Weigand, P. Agrawal, I. Lemesch, M. A. Mawass, P. Fischer, M. Kläui, and G. S. Beach, Observation of room-temperature magnetic skyrmions and their current-driven dynamics in ultrathin metallic ferromagnets, *Nat. Mater.* **15**, 501 (2016).
- [4] W. Jiang, X. Zhang, G. Yu, W. Zhang, X. Wang, M. Benjamin Jungfleisch, J. E. Pearson, X. Cheng, O. Heinonen, K. L. Wang, Y. Zhou, A. Hoffmann, and S. G. Te Velthuis, Direct observation of the skyrmion Hall effect, *Nat. Phys.* **13**, 162 (2017).
- [5] R. Juge, S.-G. Je, D. de Souza Chaves, L. D. Buda-Prejbeanu, J. Peña-García, J. Nath, I. M. Miron, K. G. Rana, L. Aballe, M. Foerster, F. Genuzio, T. O. Menteş, A. Locatelli, F. Maccherozzi, S. S. Dhesi, M. Belmeguenai, Y. Roussigné, S. Auffret, S. Pizzini, G. Gaudin *et al.*, Current-Driven Skyrmion Dynamics and Drive-Dependent Skyrmion Hall Effect in an Ultrathin Film, *Phys. Rev. Appl.* **12**, 044007 (2019).
- [6] C. Reichhardt and C. J. Olson Reichhardt, Noise fluctuations and drive dependence of the skyrmion Hall effect in disordered systems, *New J. Phys.* **18**, 095005 (2016).
- [7] Z. Chen, X. Zhang, Y. Zhou, and Q. Shao, Skyrmion Dynamics in the Presence of Deformation, *Phys. Rev. Appl.* **17**, L011002 (2022).
- [8] R. Tomasello, E. Martinez, R. Zivieri, L. Torres, M. Carpentieri, and G. Finocchio, A strategy for the design of skyrmion race-track memories, *Sci. Rep.* **4**, 6784 (2014).
- [9] F. Büttner, C. Moutafis, M. Schneider, B. Krüger, C. M. Günther, J. Geilhufe, C. V. Schmising, J. Mohanty, B. Pfau, S. Schaffert, A. Bisig, M. Foerster, T. Schulz, C. A. Vaz, J. H. Franken, H. J. Swagten, M. Kläui, and S. Eisebitt, Dynamics and inertia of skyrmionic spin structures, *Nat. Phys.* **11**, 225 (2015).
- [10] W. Legrand, D. Maccariello, N. Reyren, K. Garcia, C. Moutafis, C. Moreau-Luchaire, S. Collin, K. Bouzehouane, V. Cros, and A. Fert, Room-temperature current-induced generation and motion of sub-100 nm skyrmions, *Nano Lett.* **17**, 2703 (2017).
- [11] G. Yu, P. Upadhyaya, X. Li, W. Li, S. K. Kim, Y. Fan, K. L. Wong, Y. Tserkovnyak, P. K. Amiri, and K. L. Wang, Room-temperature creation and spin-orbit torque manipulation of skyrmions in thin films with engineered asymmetry, *Nano Lett.* **16**, 1981 (2016).
- [12] T. Dohi, S. Dutta Gupta, S. Fukami, and H. Ohno, Formation and current-induced motion of synthetic antiferromagnetic skyrmion bubbles, *Nat. Commun.* **10**, 5153 (2019).
- [13] S. Woo, K. M. Song, X. Zhang, Y. Zhou, M. Ezawa, X. Liu, S. Finizio, J. Raabe, N. J. Lee, S. I. Kim, S. Y. Park, Y. Kim, J. Y. Kim, D. Lee, O. Lee, J. W. Choi, B. C. Min, H. C. Koo, and J. Chang, Current-driven dynamics and inhibition of the skyrmion Hall effect of ferrimagnetic skyrmions in GdFeCo films, *Nat. Commun.* **9**, 959 (2018).
- [14] K. Litzius, I. Lemesch, B. Krüger, P. Bassirian, L. Caretta, K. Richter, F. Büttner, K. Sato, O. A. Tretiakov, J. Förster, R. M. Reeve, M. Weigand, I. Bykova, H. Stoll, G. Schütz, G. S. Beach, and M. Kläui, Skyrmion Hall effect revealed by direct time-resolved X-ray microscopy, *Nat. Phys.* **13**, 170 (2017).
- [15] A. Hrabec, J. Sampaio, M. Belmeguenai, I. Gross, R. Weil, S. M. Chérif, A. Stashkevich, V. Jacques, A. Thiaville, and S. Rohart, Current-induced skyrmion generation and dynamics in symmetric bilayers, *Nat. Commun.* **8**, 15765 (2017).
- [16] K. Litzius, J. Leliaert, P. Bassirian, D. Rodrigues, S. Kromin, I. Lemesch, J. Zazvorka, K. J. Lee, J. Mulkers, N. Kerber, D. Heinze, N. Keil, R. M. Reeve, M. Weigand, B. Van Waeyenberge, G. Schütz, K. Everschor-Sitte, G. S. Beach, and M. Kläui, The role of temperature and drive current in skyrmion dynamics, *Nat. Electron.* **3**, 30 (2020).

- [17] W. Jiang, P. Upadhyaya, W. Zhang, G. Yu, M. B. Jungfleisch, F. Y. Fradin, J. E. Pearson, Y. Tserkovnyak, K. L. Wang, O. Heinonen, S. G. Te Velthuis, and A. Hoffmann, Blowing magnetic skyrmion bubbles, *Science* **349**, 283 (2015).
- [18] K. Zeissler, S. Finizio, C. Barton, A. J. Huxtable, J. Massey, J. Raabe, A. V. Sadovnikov, S. A. Nikitov, R. Brearton, T. Hesjedal, G. van der Laan, M. C. Rosamond, E. H. Linfield, G. Burnell, and C. H. Marrows, Diameter-independent skyrmion Hall angle observed in chiral magnetic multilayers, *Nat. Commun.* **11**, 428 (2020).
- [19] A. K. C. Tan, P. Ho, J. Lourembam, L. Huang, H. K. Tan, C. J. O. Reichhardt, C. Reichhardt, and A. Soumyanarayanan, Visualizing the strongly reshaped skyrmion Hall effect in multilayer wire devices, *Nat. Commun.* **12**, 4252 (2021).
- [20] Y. Hirata, D. H. Kim, S. K. Kim, D. K. Lee, S. H. Oh, D. Y. Kim, T. Nishimura, T. Okuno, Y. Futakawa, H. Yoshikawa, A. Tsukamoto, Y. Tserkovnyak, Y. Shiota, T. Moriyama, S. B. Choe, K. J. Lee, and T. Ono, Vanishing skyrmion Hall effect at the angular momentum compensation temperature of a ferromagnet, *Nat. Nanotechnol.* **14**, 232 (2019).
- [21] P. Hansen, S. Klahn, C. Clausen, G. Much, and K. Witter, Magnetic and magneto-optical properties of rare-earth transition-metal alloys containing Gd, Tb, Fe, Co, *J. Appl. Phys.* **66**, 756 (1989).
- [22] E. Haltz, R. Weil, J. Sampaio, A. Pointillon, O. Rousseau, K. March, N. Brun, Z. Li, E. Briand, C. Bachelet, Y. Dumont, and A. Mougin, Deviations from bulk behavior in TbFe(Co) thin films: Interfaces contribution in the biased composition, *Phys. Rev. Mater.* **2**, 104410 (2018).
- [23] See Supplemental Material at <http://link.aps.org/supplemental/10.1103/PhysRevB.106.144408> for details on the model, current-induced parasitic phenomena, additional data including videos, and material characterization measurements.
- [24] R. K. Wangsness, Sublattice effects in magnetic resonance, *Phys. Rev.* **91**, 1085 (1953).
- [25] A. S. Kornilov and I. V. Safonov, An overview of watershed algorithm implementations in open source libraries, *J. Imag.* **4**, 123 (2018).
- [26] S. Rohart and A. Thiaville, Skyrmion confinement in ultrathin film nanostructures in the presence of Dzyaloshinskii-Moriya interaction, *Phys. Rev. B* **88**, 184422 (2013).
- [27] O. Boulle, J. Vogel, H. Yang, S. Pizzini, D. De Souza Chaves, A. Locatelli, T. O. Menteş, A. Sala, L. D. Buda-Prejbeanu, O. Klein, M. Belmeguenai, Y. Roussigné, A. Stashkevich, S. Mourad Chérif, L. Aballe, M. Foerster, M. Chshiev, S. Auffret, I. M. Miron, and G. Gaudin, Room-temperature chiral magnetic skyrmions in ultrathin magnetic nanostructures, *Nat. Nanotech.* **11**, 449 (2016).
- [28] A. Bernard-Mantel, L. Camosi, A. Wartelle, N. Rougemaille, M. Darques, and L. Ranno, The skyrmion-bubble transition in a ferromagnetic thin film, *SciPost Phys.* **4**, 027 (2018).
- [29] I. Gross, W. Akhtar, A. Hrabec, J. Sampaio, L. J. Martínez, S. Chouaieb, B. J. Shields, P. Maletinsky, A. Thiaville, S. Rohart, and V. Jacques, Skyrmion morphology in ultrathin magnetic films, *Phys. Rev. Mater.* **2**, 024406 (2018).
- [30] R. Juge, S. G. Je, D. Souza Chaves, S. Pizzini, L. D. Buda-Prejbeanu, L. Aballe, M. Foerster, A. Locatelli, T. O. Menteş, A. Sala, F. Maccherozzi, S. S. Dhesi, S. Auffret, E. Gautier, G. Gaudin, J. Vogel, and O. Boulle, Magnetic skyrmions in confined geometries: Effect of the magnetic field and the disorder, *J. Magn. Magn. Mater.* **455**, 3 (2018).
- [31] K. Zeissler, M. Mruczkiewicz, S. Finizio, J. Raabe, P. M. Shepley, A. V. Sadovnikov, S. A. Nikitov, K. Fallon, S. McFadzean, S. McVitie, T. A. Moore, G. Burnell, and C. H. Marrows, Pinning and hysteresis in the field dependent diameter evolution of skyrmions in Pt/Co/Ir superlattice stacks, *Sci. Rep.* **7**, 15125 (2017).
- [32] A. A. Thiele, Applications of the gyrocoupling vector and dissipation dyadic in the dynamics of magnetic domains, *J. Appl. Phys.* **45**, 377 (1974).
- [33] A. Salimath, A. Abbout, A. Brataas, and A. Manchon, Current-driven skyrmion depinning in magnetic granular films, *Phys. Rev. B* **99**, 104416 (2019).
- [34] S. Krishnia, E. Haltz, L. Berges, L. Aballe, M. Foerster, L. Bocher, R. Weil, A. Thiaville, J. Sampaio, and A. Mougin, Spin-Orbit Coupling in Single-Layer Ferrimagnets: Direct Observation of Spin-Orbit Torques and Chiral Spin Textures, *Phys. Rev. Appl.* **16**, 024040 (2021).
- [35] A. A. Thiele, Steady-State Motion of Magnetic Domains, *Phys. Rev. Lett.* **30**, 230 (1973).
- [36] E. Haltz, S. Krishnia, L. Berges, A. Mougin, and J. Sampaio, Domain wall dynamics in antiferromagnetically coupled double-lattice systems, *Phys. Rev. B* **103**, 014444 (2021).
- [37] G. Vella-Coleiro, Domain Wall Mobility in Epitaxial Garnet Films, *AIP Conf. Proc. No. 10* (AIP, New York, 1973), p. 424.
- [38] M. Hayashi, J. Kim, M. Yamanouchi, and H. Ohno, Quantitative characterization of the spin-orbit torque using harmonic Hall voltage measurements, *Phys. Rev. B* **89**, 144425 (2014).
- [39] D. Capic, D. A. Garanin, and E. M. Chudnovsky, Skyrmion-skyrmion interaction in a magnetic film, *J. Phys.: Condens. Matter* **32**, 415803 (2020).
- [40] R. Brearton, G. van der Laan, and T. Hesjedal, Magnetic skyrmion interactions in the micromagnetic framework, *Phys. Rev. B* **101**, 134422 (2020).
- [41] X. Zhang, Y. Zhou, and M. Ezawa, Magnetic bilayer-skyrmions without skyrmion Hall effect, *Nat. Commun.* **7**, 10293 (2016).
- [42] H. Vakili, W. Zhou, C. T. Ma, S. J. Poon, M. G. Morshed, M. N. Sakib, S. Ganguly, M. Stan, T. Q. Hartnett, P. Balachandran, J. W. Xu, Y. Quessab, A. D. Kent, K. Litzius, G. S. Beach, and A. W. Ghosh, Skyrmionics-Computing and memory technologies based on topological excitations in magnets, *J. Appl. Phys.* **130**, 070908 (2021).
- [43] F. Hellman, A. Hoffmann, Y. Tserkovnyak, G. S. D. Beach, E. E. Fullerton, C. Leighton, A. H. MacDonald, D. C. Ralph, D. A. Arena, H. A. Dürr, P. Fischer, J. Grollier, J. P. Heremans, T. Jungwirth, A. V. Kimel, B. Koopmans, I. N. Krivorotov, S. J. May, A. K. Petford-Long, J. M. Rondinelli *et al.*, Interface-induced phenomena in magnetism, *Rev. Mod. Phys.* **89**, 025006 (2017).
- [44] J. Sampaio, V. Cros, S. Rohart, A. Thiaville, and A. Fert, Nucleation, stability and current-induced motion of isolated magnetic skyrmions in nanostructures, *Nat. Nanotechnol.* **8**, 839 (2013).
- [45] A. Belavin and A. Polyakov, Metastable states of two-dimensional isotropic ferromagnets, *JETP Lett.* **22**, 503 (1975).
- [46] F. Büttner, I. Limesch, and G. S. Beach, Theory of isolated magnetic skyrmions: From fundamentals to room temperature applications, *Sci. Rep.* **8**, 4464 (2018).
- [47] A. Vansteenkiste, J. Leliaert, M. Dvornik, M. Helsen, F. Garcia-Sanchez, and B. Van Waeyenberge, The de-

- sign and verification of MuMax3, *AIP Adv.* **4**, 107133 (2014).
- [48] E. Haltz, J. Sampaio, S. Krishnia, L. Berges, R. Weil, and A. Mougin, Measurement of the tilt of a moving domain wall shows precession-free dynamics in compensated ferrimagnets, *Sci. Rep.* **10**, 16292 (2020).
- [49] E. Haltz, J. Sampaio, S. Krishnia, L. Berges, R. Weil, A. Mougin, and A. Thiaville, Quantitative analysis of spin wave dynamics in ferrimagnets across compensation points, *Phys. Rev. B* **105**, 104414 (2022).
- [50] C. Eylich, A. Zamani, W. Huttema, M. Arora, D. Harrison, F. Rashidi, D. Broun, B. Heinrich, O. Mryasov, M. Ahlberg, O. Karis, P. E. Jönsson, M. From, X. Zhu, and E. Girt, Effects of substitution on the exchange stiffness and magnetization of Co films, *Phys. Rev. B* **90**, 235408 (2014).
- [51] T. Katayama, K. Hasegawa, K. Kawanishi, and T. Tsushima, Annealing effects on magnetic properties of amorphous GdCo, GdFe, and GdCoMo films, *J. Appl. Phys.* **49**, 1759 (1978).
- [52] T. Devolder, P.-H. Ducrot, J.-P. Adam, I. Barisic, N. Vernier, J.-V. Kim, B. Ockert, and D. Ravelosona, Damping of $\text{Co}_x\text{Fe}_{80-x}\text{B}_{20}$ ultrathin films with perpendicular magnetic anisotropy, *Appl. Phys. Lett.* **102**, 022407 (2013).